Melting in the Fe-C system to 70 GPa

O.T. Lord[a]*, M.J. Walter[a], R. Dasgupta[b,1] D. Walker[b], S.M. Clark[c]

[a]*Department of Earth Sciences, University of Bristol, Wills Memorial Building, Queen's Road, Bristol, BS8 1RJ, UK*

[b]*Lamont-Doherty Earth Observatory, P. O. Box 1000, 61 Route 9W, Palisades, NY 10964-1000, USA*

[c]*Advanced Light Source, Lawrence Berkeley National Lab., MS6R2100, 1 Cyclotron Road, Berkeley, CA 94720-8226, USA*

*Corresponding Author

Email: Oliver.Lord@bristol.ac.uk

Phone: +44 117 3315194

Fax: +44 117 9253385

Total number of words in Main text: 6560

Abstract: 349

Number of figures: 10

Number of Supplementary figures: 3

Number of Supplementary tables: 1

References: 59

---

[1]Present Address: *Department of Earth Science, Rice University, 6100 Main Street, MS-126, Houston, Texas 77005, USA*

Abstract

We determined high pressure melting curves for Fe_3C, Fe_7C_3 and the Fe–Fe_3C eutectic using laser-heated diamond anvil cell techniques. The principle criterion for melting is the observation of plateaus in the temperature vs. laser power function, which is an expected behavior at isobaric invariant points (e.g. congruent, eutectic, or peritectic melting) as increased power provides the latent heat of melting. We verified this technique by reproducing the melting curves of well-studied congruently melting compounds at high pressure (Fe, Pt, FeS, Pb), and by comparison with melting determinations made using thermocouple-based large volume press techniques. The incongruent melting curve of Fe_3C measured to 70 GPa has an apparent change in slope at ~8 GPa, which we attribute to stabilization of Fe_7C_3 at the solidus and the creation of a *P-T* invariant point. We observe that Fe_7C_3 melts at higher temperatures than Fe_3C between 14 and 52 GPa and has a steep *P-T* slope, and on this basis predict an expanding field of Fe_7C_3 + liquid with pressure. The Fe-Fe_3C eutectic melting curve measured to 70 GPa agrees closely with multi-anvil data and thermodynamic calculations. We also measured the eutectic composition as a function of pressure using an in situ X-radiographic imaging technique, and find a rapid drop in carbon in the eutectic composition above about 20 GPa, generally consistent with previous thermodynamic calculations, and predict that the eutectic lies close to pure iron by ~50 GPa. We use these observations to extrapolate phase relations to core-relevant pressures. Convergence of the Fe_3C and Fe-Fe_3C eutectic melting curves indicate that Fe_3C is replaced at the solidus by Fe_7C_3 at ~120 GPa, forming another *P-T* invariant point and a new eutectic between Fe and Fe_7C_3. Thus, Fe_3C is unlikely to be an important crystallizing phase at core conditions, whereas Fe_7C_3 could become an important crystallizing phase.

Keywords: Carbon; core; iron carbide; light element

1. Introduction

The composition of Earth's core has long been subject to controversy. Measurements of the room temperature equation of state of pure iron and iron-nickel alloys to two megabars and beyond (Dewaele et al., 2006; Mao et al., 1990) have consistently yielded higher densities than predicted from geophysical models (Birch, 1952; 1964). Although thermal expansion at the temperatures likely to be relevant to the core partially mitigates the problem (Alfè et al., 2004; Boehler, 1993; Luo and Ahrens, 2004; Ma et al., 2004; Shen et al., 1998), recent determinations of the thermal equation of state of iron at high pressures (Dubrovinsky et al., 2000), extrapolated to core temperatures, still leaves the core insufficiently dense. Recent estimates of the core density deficit range from 3-10% for the outer core (Anderson and Isaak, 2002; Shanker et al., 2004) and 2.5-9% for the inner core (Dewaele et al., 2006; Dubrovinsky et al., 2000), although the magnitude of the deficit depends strongly on the chosen thermal profile.

Several possible contenders have been proposed for the alloying elements, including hydrogen, carbon, oxygen, silicon and sulfur (Poirier, 1994), with the popularity of each waxing and waning, and some mixture seems most likely (e.g. Alfè et al., 2002; Badro et al., 2007; McDonough, 2003). Constraining the composition of the core is critical if we are to better understand it's thermal structure and crystallization history, dynamo action, energy balance, postulated interaction with the mantle, and the partitioning of siderophile elements (Buffett et al., 2000; Chabot et al., 2006; Jana and Walker, 1997; Lister and Buffett, 1998; Walker, 2005). Although a great deal has been achieved in this area (e.g.: Li & Fei, 2003), much remains to be determined about the relevant iron-light element phase diagrams at pressures relevant to the core's formation and it's present state.

Carbon is the fourth most abundant element in the solar system, with the CI chondrites containing 3.5 wt% C (Lodders, 2003). The potential importance of carbon in the cores of the terrestrial planets is suggested by the presence of both graphite and cohenite $(Fe,Ni)_3C$ in iron meteorites (e.g.: Goodrich, 1992). It is estimated that the bulk silicate Earth has about 120 ppm

53 (McDonough and Sun, 1995) to 400 ppm (Javoy, 1997) carbon, which is a small amount when
54 compared to the chondrites. Whether this mismatch reflects a low overall abundance in Earth due to
55 volatile loss during accretion or to sequestration into the core during core formation is an open
56 question. As a result of these difficulties, estimates of the Earth's carbon content are speculative and
57 diverse, ranging from as low as 0.2 wt% (Dasgupta and Walker, 2008; McDonough, 2003) to 4
58 wt% (Hillgren et al., 2000). Carbon is thus a potential and interesting candidate for at least part of
59 the light element budget of the core, which makes understanding the Fe-C phase diagram at high
60 pressures a priority.

61 The iron-rich portion of the Fe-C binary system has been studied extensively at 1 atm and
62 modest pressures due to its importance in metallurgy (e.g. Chipman, 1972; Strong and Chrenko,
63 1971), as shown in Fig. 1. At 1 atm (Fig. 1a) there is a eutectic, possibly metastable, between iron
64 and graphite at 1420 K and 4.3 wt% carbon. The compound, Fe_3C (cementite), melts incongruently
65 to liquid + graphite at about the eutectic temperature. At higher pressure (e.g. 5.7 GPa; Fig. 1b),
66 Fe_3C melts in a peritectic reaction to form liquid + diamond, and a eutectic exists between Fe and
67 Fe_3C. At higher pressures still another important compound, Fe_7C_3, stabilizes and is known to melt
68 incongruently to liquid + diamond at 9 GPa (Shterenberg et al., 1975; Tsuzuki et al., 1984).

69 Wood (1993) calculated phase relations up to 136 GPa in the Fe-C system on the basis of a
70 thermodynamic model, and predicted that pressure would cause a decrease in the carbon content of
71 the eutectic between Fe and Fe_3C, with the carbon content becoming negligible at core pressures.
72 This was predicted to occur because of a rapid increase in the melting point of Fe_3C and a
73 consequent expansion of the Fe_3C + liquid field. Wood (1993) also predicted that Fe_3C melts
74 incongruently at low pressures to liquid + graphite, but that melting becomes congruent by 15 GPa.
75 Thus, for a planetary core in which the entire light element budget consists of carbon, the inner core
76 would consist of pure Fe_3C, with a residual outer core liquid that would have decreasing carbon
77 content as crystallization progressed. However, neutron diffraction measurements (Wood et al.,
78 2004) and ab initio calculations (Vocadlo et al., 2002) have established that the effect of the

ferromagnetic to paramagnetic transition in Fe_3C (Häglund et al., 1991) changes its thermoelastic parameters relative to those used by Wood (1993). These changes are expected to substantially reduce the high-pressure stability field of Fe_3C, calling the predicted phase relations into question. Further, the presence of Fe_7C_3, which becomes stable above 6 GPa (Shterenberg, 1975; Tsuzuki et al., 1984; Nakajima et al., in press), may also affect the phase diagram in ways not fully captured by the earlier modeling of Wood (1993).

Here we investigate melting phase relations at high pressures in the system Fe-C to further test the proposed phase relations of Wood (1993), corroborate more recent large volume press studies, and extend our knowledge of the Fe-C system to pressures more relevant to the core. Specifically, we have measured the first melting curves of Fe_3C, Fe_7C_3 and the Fe-Fe_3C eutectic to ~70 GPa using the laser-heated diamond anvil cell (LHDAC), and determined the eutectic composition in situ to 44 GPa using a novel X-radiographic imaging technique (Walker et al., 2009). We also report piston-cylinder and multi-anvil quench determinations of Fe_3C melting at lower pressures. We use these data to construct phase diagrams for the Fe-C binary at high pressures, and to assess the role of carbon-rich phases during core crystallization in Earth.

2. Experimental Methods

High-pressure melting experiments were made in symmetric diamond anvils cells (DAC) using diamonds with 200–300 μm diameter culets. Samples were loaded into 80–130 μm holes drilled in stainless steel or rhenium gaskets pre-indented to ~50 μm thickness. In conjunction with the DAC experiments, several synthesis and melting experiments were made in piston-cylinder and multi-anvil apparatus at Lamont-Doherty Earth Observatory (LDEO), for which the details of the experimental methods can be found elsewhere (Dasgupta and Walker, 2008).

105 *2.1 Fe_3C and Fe_7C_3 Melting Experiments*

106 The Fe_3C starting material was synthesized from pure iron wire placed in a graphite capsule
107 and held for 2 days at 2 GPa and 1473 K in a piston cylinder apparatus. The Fe_7C_3 starting material
108 was synthesized at 7 GPa and 1623 K for 7 minutes in a multi-anvil press using the same method as
109 for the Fe_3C. Both syntheses were carried out at LDEO, and phase purity was confirmed for each by
110 XRD and EPMA (Dasgupta and Walker, 2008). Starting materials were ground under ethanol in an
111 agate mortar to produce a fine powder with a grain size of ~3 μm, and then compressed into a dense
112 foil with a thickness of ~10–15 μm. Fragments of these foils were used as samples instead of loose
113 powder to minimize sample deformation and thickness variations during compression. Starting
114 materials were placed in an oven at 125 °C for at least one hour before loading. The carbide foils
115 were loaded into a gasket hole between thermal insulating layers to allow efficient heating of the
116 sample, to minimise temperature gradients, and to act as the pressure medium. We used several
117 kinds of insulators including single-crystal sapphire discs (125 μm in diameter and 15-20 μm thick),
118 dense foils of ruby powder (10-15 μm thick), sol gel deposited Al_2O_3, and NaCl. Dubrovinsky et al.
119 (2001) observed the formation of Fe_3Al and an Fe-Al alloy when iron and Al_2O_3 were reacted in the
120 LHDAC above 60 GPa, but we observe no such phases in our experiments in Al_2O_3 at similar
121 conditions, based on synchrotron X-Ray Diffraction data. NaCl is preferred because it has a low
122 shear strength, which promotes quasi-hydrostatic conditions in the sample chamber at high
123 pressures and minimizes the pressure drop on heating caused by stress relaxation, but can only be
124 used at higher pressures (e.g. > 40 GPa) where the NaCl melting curve rises above that of the
125 samples (Boehler et al., 1997). A recent study by Rouquette et al. (2008) indicates that iron heated
126 at 2700 K and 58 GPa in the LHDAC using NaCl insulators reacts to form Fe_3C, suggesting NaCl is
127 not impervious to carbon diffusion. We see similar results in XRD analyses of quenched iron
128 melting experiments using NaCl (but not Al_2O_3), though the amount of Fe_3C produced is very
129 small. However, when different insulators are used over a similar pressure range, we find no
130 resolvable dependence of melting temperatures on the pressure medium.

Melting experiments on Fe_3C were also carried out at 2 to 6 GPa using a piston cylinder (PC: 2±0.1 GPa: Dasgupta and Walker, 2008) and a Walker-style multi-anvil apparatus (MA: 5±0.5 and 6±0.5 GPa) at LDEO. All the experiments employed 1.5-2.0 mm long pure Fe wire of 1 mm diameter in graphite capsules as starting materials. The piston cylinder experiments used a standard ½" assembly with $BaCO_3$ pressure cell, graphite external heater, and crushable MgO spacers. The multi-anvil experiments were conducted using 8 mm truncation edge length WC cubes, castable MgO octahedral assemblies with $LaCrO_3$ heaters, and MgO spacers. Temperature during both the PC and the MA experiments was monitored using $W_{97}Re_3/W_{75}Re_{25}$ thermocouples placed against the capsule wall with uncertainties of ±10 K and ±15 K respectively. Polished sections of the quenched run products were studied by electron probe microanalysis.

2.2 Fe-Fe_3C Eutectic Melting Experiments

Eutectic melting experiments as well as in situ X-Radiographic imaging (XRI) experiments to determine the eutectic composition in the Fe-C system are made by melting at the boundary between spatially resolved ingredients of pure iron metal and Fe_3C (Walker, 2005; Walker et al., 2009). The following procedure is found to achieve a well defined and stable boundary even at high sample compression: (1) Pure hardened iron foil is indented in a DAC to ~15 GPa, which yields a metal thickness of ~20 μm. (2) The indented metal is then drilled with 50 μm holes, which are loaded with powdered Fe_3C and compressed until the material is sufficiently compacted to remain in place. (3) An ~100 μm diameter 'donut' consisting of the central plug of Fe_3C and a thin annulus of iron is then cut out using an UV laser. The donut with stuffing is then polished using 1 μm diamond-impregnated Mylar, cleaned under acetone and stored in an oven at 125°C until loading, typically between insulating muffins of sol gel bound Al_2O_3. The sample is then laser-heated at the boundary until first melting occurs as described in section 2.4.

157 *2.3 Pressure measurement*

158 Samples were compressed and pressure monitored using the ruby fluorescence scale as
159 calibrated by Mao et al. (1986). Several ruby grains ~3–5 μm in diameter were placed within the
160 sample chamber in early experiments, although we eventually opted for a thin layer of sub-micron
161 ruby spread across the chamber in order to measure pressure exactly at the melted spot. Pressure
162 was measured before and after melting. We assume that the post-melting pressure represents a
163 minimum estimate of the pressure at melting, as no correction for thermal pressure has been made
164 due to the uncertainty in its estimation. Samples were heated at subsolidus temperatures for several
165 minutes before melting, which reduces considerably radial pressure gradients that can develop
166 during initial compression. Measured pressure gradients across the sample chamber after melting,
167 were generally less than ~1 GPa. Pressure losses of ~5 GPa due to annealing of stresses were
168 observed in experiments using sol-gel Al_2O_3, compared to <2 GPa when using NaCl. The use of
169 single-crystal sapphire resulted in a drastic pressure drop on annealing of ~10 GPa, and so it was
170 abandoned as a pressure medium.

171 The biggest source of uncertainty in the reported pressures is the thermal pressure. Recent in
172 situ melting experiments by Dewaele et al. (2007) using NaCl as a pressure medium indicate
173 thermal pressures at melting of <3 GPa. However, because Al_2O_3 is much harder than NaCl, the
174 thermal pressure in these experiments is likely to be greater and is a positive function of
175 temperature, regardless of the medium employed. Therefore, while the pressures reported here have
176 analytical uncertainties on the order of ±1-2 GPa it should be born in mind that these represent
177 minima, underestimating the true pressure by perhaps 3-5 GPa.

178

179 *2.4 Laser heating and temperature measurement*

180 Samples were heated at pressure in a double-sided heating geometry using either a 50 W
181 Nd:YLF CW infrared laser operating in TEM_{01} mode, or a 100 W Nd:YAG CW multimode laser.
182 This system produced stable heated spots with diameters of ~20–40 μm. The incandescent light

183 emitted from the sample was monitored using CCD cameras for visual observation on both sides.
184 The temperature was raised in the sample by increasing the laser power in small increments
185 (typically < 1 watt).

186 Temperatures were measured spectroradiometrically on one side using standard techniques
187 employed at Bristol as described in detail elsewhere (Walter and Koga, 2004). In brief, a magnified
188 image of the heated spot (20x) is focused onto the entrance slit (40 μm width) of an imaging
189 spectrometer equipped with a 2-D CCD (e.g. 1024 x 256 pixels). We pre-align the system so that
190 the image of the heated spot is centered on the slit. This allows sampling of a 'one-dimensional'
191 temperature profile across the heated spot with a spatial resolution of ~2 μm^2 (see Supplemental
192 Figure 1).

193 The precision of spectroradiometric temperature measurement is dependant upon the
194 closeness of the fit of the measured spectrum to the Planck or Wien blackbody function (Heinz and
195 Jeanloz, 1987; Kavner and Panero, 2004; Walter and Koga, 2004). Replicate analyses of the
196 calibration lamp yield maximum instrumental precision in temperature measurement of ~0.1%
197 relative (note that temperatures measured using the W lamp as an unknown are not subject to
198 chromatic effects because the lamp is at constant temperature across the field of view).

199 Another potential source of uncertainty in both the precision and accuracy of measured
200 temperatures is the chromatic dispersion introduced by the optical elements in the path to the
201 spectrometer, which can have a large effect on calculated temperatures when a steep temperature
202 gradient is present (Benedetti et al., 2007; Boehler, 2000; Walter and Koga, 2004). However,
203 effective mitigation of chromatic effects can be achieved by placing an f-stop between the objective
204 and focusing lens to sample only the near-paraxial rays that produce very little dispersion, and by
205 choosing a wavelength range appropriate for the lens system (Benedetti et al., 2007; Walter and
206 Koga, 2004). An example of fitted spectra and the resulting temperature profile across a laser-
207 heated spot produced at optimum configuration is shown in Supplemental Figure 1. In our melting

experiments the precision in the fits to the Wien or Planck functions is typically in the range of 0.1-0.4%, which indicates that chromatic effects are virtually eliminated.

To further assess the accuracy of our system we have measured the melting points of Pt, Nb, Mo, Ta, Re and W at 1 atm. A pure metal filament is resistively heated in an Ar gas chamber. Temperature is increased incrementally using a radiometric power supply, and is measured spectroradiometrically at the hot spot of the filament. When melting occurs, the filament breaks, and we estimate the melting temperature from the power-temperature path. Supplemental Figure 2 shows the results of replicate analyses of melting points for these metals. Relative to published melting data our results indicate a systematic overestimation of temperature by about 50 to 200 K for these metals. These differences may be a consequence of metal-specific deviations from wavelength independent emissivity ('greybody' behavior). We do not attempt to assign any formal uncertainty in accuracy to our measurements at this point, but caution that uncorrected deviations from greybody behavior will likely cause an overestimation in temperature of the order tens to a few hundred degrees K.

2.5 Melt detection

We rely on discontinuities in the temperature vs. laser power function to detect the onset of melting. During laser heating, when a sample reaches an invariant melting point, for example at a binary eutectic or peritectic, the temperature should plateau at the invariant temperature as the laser power provides the latent heat of melting. That is, increasing laser power serves only to increase the volume of melt rather than raise the temperature of the molten material, at least until a certain melt threshold is reached. We have observed that such melting discontinuities are easily and reproducibly detectible, and several typical examples are shown in Fig. 2. Figure 2a shows a common pathology in which peak temperature increases monotonically with laser current (i.e. power) until a threshold is reached, after which further power causes a temperature plateau with fluctuations often of the order ±50 K. In this particular case during heating of Fe_3C at 43 GPa, we

234 estimate the melting temperature by averaging over the points within the plateau, yielding 2650 K.
235 The assigned uncertainty is derived to encompass the analytical precision in temperature
236 measurement (usually 3-10 K), the position of the plateau (usually 10-50 K) and the temperature
237 gradient within the heated spot (estimated at 40 K), in this case yielding a total of ± 98 K. Figure 2b
238 shows another example in which a long plateau is reached after an initial temperature perturbation
239 during heating at the junction of Fe-Fe_3C at 70 GPa. In this case we estimate melting at 2630 ± 40
240 K. A final and less common example is shown in Fig. 2c, in which a single, large temperature
241 discontinuity occurs after a very systematic increase in temperature, and based on extrapolation we
242 estimate melting at 2970 ± 55 K. We suggest that such large perturbations are related to the loss of
243 the sample's shear strength upon melting leading to a considerable change in sample absorption (as
244 evidenced by holes in the sample foil after experiments in which this behaviour was observed), but
245 consider this melting criterion less robust as such failure could be related to subsolidus softening.
246 However, we have produced consistent melting points in replicate experiments in which both
247 plateaus and extreme perturbations have been used as melting criteria.

248 As a means of validating our melting criteria we have measured the melting curves of Fe, Pt,
249 FeS and Pb at pressures from 5 to 45 GPa (~1900 to 2600 K), and these data are compared to data
250 from previous studies in Figure 3. Our melting curve for pure Fe closely matches the melting curve
251 of Boehler (1993), which was determined in an LHDAC using visual identification of melt motion
252 as a melting criterion. We also have acceptable correspondence with the data of Ringwood and
253 Hibberson (1990) that is based on thermocouple temperature measurement in a large-volume
254 apparatus. Overall our melting data show excellent consistency with previously measured melting
255 curves in all cases (Boehler, 1992; Boehler, 1993; Dewaele et al., 2007; Kavner and Jeanloz, 1998).
256 Further, we show below that where our new data overlaps most observations made in large volume
257 apparatus we find good correspondence.
258
259

2.6 Eutectic melt composition by X-radiography

Determining the composition of a eutectic melt has thus far only been possible by ex situ analysis of quenched run products. However, due to the potential for exsolution of the light element from the melt during cooling, especially in slower quenching large-volume apparatus, re-integration of the melt composition is at best an uncertain task (O'Neill et al., 1998; Walker, 2005). Variation in quench rate among different-sized pressure cells may also contribute to error in measured melting curves (Walker, 2005). DAC experiments quench orders of magnitude more rapidly than large-volume experiments, but it is not clear whether exsolution can still cause problems in analysis. A compounding problem is the intrinsic difficulty in making accurate electron probe or TEM-EDX measurement of carbon in DAC samples. Clearly, an in situ method is preferable. For example, in the recent work of Seagle et al. (2008) the composition of liquids was bounded by in situ XRD determination of phase disappearance with temperature for particular bulk compositions. Another method for direct determination of liquid composition is to melt at the boundary between spatially resolved components (e.g. Fe and Fe_3C) and simultaneously measure the X-ray transmission through the sample. For a binary system, the transmissivity should be a simple function of density and, therefore, composition for samples of uniform thickness. By linear interpolation between the observed transmissivity of the pure solid end member compositions, the transmissivity of the molten regions can potentially yield the melt composition directly (Walker et al., 2009; Walker, 2005). Walker et al. (2009) tested this method in the system Fe-S where the change in eutectic melt compositions is well documented to ~30 GPa, and found excellent reproducibility of known results.

Fe-Fe_3C melting experiments were prepared as described above and were heated at beam-line 12.2.2 of the Advanced Light Source, which utilizes a double-sided heating similar to the Bristol system (Caldwell et al., 2007). Temperature measurement and melt detection was identical to the method described above. In all cases melting occurred within error of the melting curve constructed using the Bristol system. During the experiment the sample was bathed in a wide beam

of high energy X-rays (~18 KeV). Transmitted X-rays were then converted to visible light via a $CdWO_4$ phosphor, which was focused onto a high-resolution CCD camera. Images were taken before, during and after melting at each laser power increment with simultaneous temperature measurement. After acquisition, cross-sections through the images were taken normal to the boundary at the melting location, and the average transmissivity of solid Fe, solid Fe_3C and melt estimated. These values were then used to calculate the composition of the melt. For a detailed description of this technique, see Walker et al. (2009).

3. Results

3.1 The Fe_3C melting curve

Figure 4a shows our melting data for Fe_3C from both diamond anvil and large-volume press experiments (see Supplementary Table). In the piston-cylinder and multi-anvil experiments at 2, 5 and 6 GPa, melting was bracketed by textural analysis of quenched run products. Below the melting temperature, coarse crystalline Fe_3C was the sole phase present in graphite capsules, and above the melting point Fe_3C crystals coexisted with a quenched Fe-C melt, formed of dendritic iron and interstitial Fe_3C (see also Dasgupta and Walker, 2008). The carbon content of the quenched melt, near the Fe_3C out point was determined by EPMA and is 5.7 wt% at 2 GPa (Dasgupta and Walker, 2008), 5.7±0.1 wt% at 5 GPa, and 5.8±0.2 wt% at 6 GPa, which confirms a peritectic melting behavior of cementite to 6 GPa. Overall, our DAC melting determinations at similarly low pressures compare favorably with experiments in large volume apparatus (Fig 4b insert). The melting data have been fitted using the empirically derived Simon equation,

$$T_m = \left[\left(P_m / A + 1 \right)^{1/C} \right] \bullet T_0$$

where T_m is the high-pressure melting point, T_0 is the ambient pressure melting point, P_m is the pressure at melting and the coefficients A and C are constants (Simon and Glatzel, 1929). This

312 equation is employed for convenience of extrapolation only, as it has no definite physical basis and
313 is of doubtful applicability to an incongruently melting substance. A single, anomalously low
314 melting point at 60 GPa has been omitted from the fit. The melting slope rises steeply up to ~10
315 GPa and then flattens off at higher pressures. The Simon fit smoothes this transition, but the fit in
316 the 10–30 GPa region is imperfect and suggests the possibility of a change in slope. We fitted the
317 data using the Kraut-Kennedy equation (Kraut and Kennedy, 1966), which predicts a linear
318 relationship between the melting temperature and the degree of isothermal compression,
319
320 $$T_m = T_0(1 + C\Delta V / V_0)$$
321
322 where ΔV is the difference between the zero pressure volume, V_0, and the volume at the pressure of
323 melting of the crystalline phase. The constant, C, is equivalent to $2\gamma_{TH} - 2/3$ where γ_{TH} is the
324 thermal Grüneisen parameter (Hofmeister & Mao, 2003). As with the Simon equation, we employ
325 this formulation for convenience. The absence of a definite physical basis for this form providing a
326 meaningful proxy for pressure and its doubtful applicability to an incongruently melting compound,
327 renders this convenience in making the point about the kink in slope in Fig. 4 at some sacrifice in
328 theoretical purity. The high pressure volumes were calculated using a third order Birch-Murnaghan
329 equation of state, with the parameters $V_{0,483}$, $K_{0,483}$ and $K'_{0,483}$ taken from the ab initio calculations
330 of Vocadlo et al. (2002) for the high temperature (>483 K) paramagnetic phase of Fe_3C relevant
331 here. The results of this analysis are shown in Fig. 4c, and a break in slope in the region of 10 GPa
332 is evident. This change in the melting slope likely corresponds to the required presence of two
333 invariant points along the Fe_3C melting curve, one corresponding to the assemblage Fe_3C + graphite
334 + diamond + liquid, and another corresponding to the assemblage Fe_3C + Fe_7C_3 + diamond + liquid.
335 We describe these phase relations in more detail in the Discussion section below.
336 Above 10 GPa, our melting curve for Fe_3C is lower than that predicted by the
337 thermodynamic calculations of Wood (1993), the discrepancy reaching ~900 K by 70 GPa. The

reason for the discrepancy between the calculated and measured melting curves may relate to the magnetic transition in Fe_3C, which is a metallic ferromagnet at 1 atmosphere and 300 K (Tsuzuki et al., 1984) but is paramagnetic above the Curie temperature of 483 K (Häglund et al., 1991). Several studies have determined the pressure of this transition at 300 K: 25 GPa from X-ray Emission Spectroscopy (Lin et al., 2004), 10 GPa from X-ray Circular Dichroism measurements (Duman et al., 2005) and 4.3 – 6.5 GPa from Synchrotron Mössbauer Spectroscopy (Gao et al., 2008). Finally, ab initio calculations predict this transition to occur above 60 GPa at 0 K (Vocadlo et al., 2002). These studies also indicate considerable changes in thermoelastic properties across the transition. For example, the 1 atm neutron diffraction data of Wood et al. (2004) show a distinct rise in the coefficient of thermal expansion above the magnetic transition. At high temperatures and pressures, the relevant phase is the non-magnetic form that has a higher bulk modulus and coefficient of thermal expansion, which would tend to reduce the Fe_3C stability field. This seems the most likely explanation for the substantial mismatch between the calculated melting temperatures of Wood (1993) and the measured values presented here.

3.2 Fe-Fe_3C eutectic

Figure 5 shows the Fe-Fe_3C eutectic melting *P-T* curve as determined using the 'donut' technique in the LH-DAC at Bristol and the ALS, fitted using the Simon equation (see Supplemental Table). Data from both laser-heating systems agree closely, and our melting curve is in excellent agreement with the multi-anvil quench data of Fei et al. (2007). At all pressures, the data are slightly below the calculated values of Wood (1993) but within mutual error. Only the low-pressure multi-anvil quench data of Hirayama et al. (1993) are anomalous relative to our melting curve.

An example showing the temperature plateau behavior and demonstrating our ability to produce a eutectic melt at the boundary between Fe and Fe_3C is shown in Fig. 6. Heating across the boundary at subsolidus temperatures produces a bi-modal temperature profile with a high-

364 temperature peak on the Fe_3C side of the boundary, as this material heated preferentially to pure Fe.
365 Increased laser power resulted in an eventual plateau in the peak temperature on the Fe_3C side
366 coincident with an increase in temperature on the Fe side. As power was increased further, the
367 temperature on the Fe side rapidly caught up to that on the Fe_3C side, and a stable plateau formed
368 across the boundary that was maintained upon further heating, which we interpret as the eutectic
369 temperature. This example is also very informative because it was taken during X-radiographic
370 imaging at beamline 12.2.2. The observed eutectic melting behaviour corresponds exactly with the
371 emergence of the ledge shown on Fig. 7b as described below, giving us confidence in both the
372 melting criterion and the interpretation of the ledge as a eutectic melt.

373 We have measured the composition of the eutectic liquid between 10 and 44 GPa using the
374 X-radiographic imaging technique described briefly above and in detail in Walker et al. (2009).
375 Figure 7 shows X-ray transmission cross-sections across the laser-heated spot for experiments at 10,
376 19 and 27 GPa. The first panel shows the precipitous drop in transmissivity across the boundary
377 between the Fe_3C plug and iron annulus of the donut before heating. The second panel shows the
378 formation of ledges of intermediate composition that formed at high temperature, representing the
379 formation of a pool of eutectic liquid between the two components. Axial temperature gradients
380 within the sample, probably on the order of 200 K (Campbell et al., 2007), may result in a non-
381 cylindrical melt pool. This interleaving of melt and solid along the X-ray transmission direction
382 may explain in part why the solid/liquid boundaries in the X-ray transmission cross-sections are not
383 perfectly sharp. Linear interpolation of the transmissivity corresponding to the in situ ledges
384 between the transmissivities of the end members yields compositions for the ledges, which are
385 plotted for all experiments in Figure 8. The data show no statistically measurable change in the
386 eutectic composition until ~20 GPa, at which point there is a rapid decrease in the eutectic
387 composition to 37 GPa. An experiment carried out at 44 GPa failed to form a detectible ledge even
388 though the melting point was reached and exceeded, which may indicate that the eutectic
389 composition dropped below the detection limit of the technique (~0.6 wt%) as determined using the

method described in Walker et al. (2009). Our results are in good agreement with the multi-anvil quench data of Chabot et al. (2008) and Hirayama et al. (1993) to 12 GPa. Preliminary results of Fei et al. (2007) indicate little change or a slight reduction in eutectic C content to 20 GPa. The uncertainties in our results and those of Fei et al. (2007) (Fei, personal communication) are such that data from these two studies overlap.

The interpretation of the XRI data assumes that the intermediate ledge represents a eutectic liquid and not an Fe-C alloy produced by diffusion, and that the region of the transmission profile taken to represent pure Fe remains so. It is our contention that these assumptions are valid for three reasons: (1) Profiles across the heated region at sub-solidus temperatures show no change in shape compared to profiles taken at 300 K; (2) The observed ledges form immediately the temperature reaches the eutectic melting curve as determined from separate off-line experiments (described above; see figure 6) and do not evolve slowly with time as would be expected for diffusion; (3) The regions used to determine the end-member compositions to which the liquid is compared are well outside the heated region, and thus should not be subject to diffusion. On this basis, we believe the drop in the carbon content of the eutectic with pressure is real, and not the result of an increasing solubility of carbon in solid iron with pressure. Our confidence in the imaging technique is established by the successful determination of the pressure dependence of the composition of the eutectic in the Fe-S system, in which excellent agreement was found with the literature (Walker et al., 2009).

Wood (1993) predicted a rapid drop in eutectic carbon content with pressure, from 4.3 wt% C at 1 atm to 2.2 wt% C at 15 GPa. Extrapolation of that trend led Wood (1993) to predict a negligible carbon content at core relevant pressures. The decrease in eutectic composition we observe is similar to the prediction of Wood, although shifted to somewhat higher pressures. Chabot et al. (2008) and Hirayama et al. (1993) found no evidence for a change in the eutectic carbon content up to 5 GPa and 12 GPa respectively, consistent with our results. Fei et al. (2007) observed

no significant pressure dependence of the eutectic composition in multi-anvil experiments up to 20 GPa, within mutual error of our results.

3.2 Melting of Fe_7C_3

We measured the melting curve of Fe_7C_3 from 14 to 52 GPa (Fig. 5). The melting curve has a relatively steep slope compared to Fe_3C, such that by 50 GPa the melting point is about 500 K higher. In contrast, Wood (1993) predicted the two phases would have similar melting points at core conditions. Shterenberg et al. (1975) show that Fe_7C_3 melts incongruently to form diamond + liquid at 9 GPa and ~1950 K, eclipsing the Fe_3C melting temperature. The phase relations at 10 GPa shown by Nakajima et al. (in press) are consistent with this interpretation. Based on these observations we predict that in *P*-*T* space the Fe_7C_3 melting curve emerges from the Fe_3C melting curve at ~8 GPa from a *P*-*T* invariant point, as described below. We note, however, that while the temperature range of the Fe_7C_3 + liquid field determined here between 15 and 25 GPa is consistent with that measured using in situ XRD in the multi-anvil experiments of Nakajima et al. (in press), their absolute melting temperatures for both phases are considerably lower than those reported here (Fig. 4a). It is noteworthy that in the experiments of Nakajima et al. (2007) iron was loaded into graphite capsules, with no control on the system bulk composition during the experiment (i.e. the capsule becomes part of the system). This conceivably provides an explanation for why the melting temperatures for Fe_3C of Nakajima et al. (in press) coincide so closely with the eutectic temperatures determined in the this study using the LHDAC and in the multi-anvil study of Fei et al. (2007). As already mentioned, our own piston cylinder and multi-anvil experiments closely corroborate our Fe_3C melting temperatures determined in the LHDAC.

4. Discussion

4.1 The Fe-C system at high pressure

The data presented above are used to construct temperature-composition phase diagrams for the iron-rich portion of the Fe-C system from 5 to 130 GPa, shown in Figure 9. Phase relations for the composition Fe_3C are summarized in a pressure-temperature isopleth in Figure 10.

At 5 GPa, Fe_3C melts incongruently to liquid + graphite at a temperature about 270 K above the Fe-Fe_3C eutectic (Fig. 9a). The shape of the liquidus is constrained by the eutectic composition, which is unchanged from its one atmosphere composition at this modest pressure (Chabot et al., 2008), and the measured composition of the peritectic liquid. It is possible that Fe_7C_3 is stable in the subsolidus at this pressure, breaking down to Fe_3C + graphite, as shown schematically. At slightly higher pressure graphite transforms to diamond, as shown in Fig. 1b (Strong and Chrenko, 1971), forming another liquidus invariant point at higher temperature. The intersection of the Gr + liquid to Di + liquid curve with the Fe_3C melting curve forms an invariant point in *P-T* space where four phases coexist (Fe_3C, Gr, Di, and liquid), and this is denoted as I1 in Fig. 10. Between 5 and 10 GPa Fe_7C_3 stabilizes and its melting temperature reaches that of Fe_3C, which corresponds to another invariant point in *P-T* space (point I2 in Fig. 10; See Supplemental Fig. 3a) where Fe_3C, Fe_7C_3, Di, and liquid coexist. We estimate the position of invariant point I2 at ~8 GPa. At pressures higher than 8 GPa the Fe_7C_3 melting point exceeds that of Fe_3C, creating a new peritectic reaction where Fe_3C melts to form Fe_7C_3 + liquid (Fig. 9b). We show this peritectic at 10 GPa (Fig. 9b) and place the peritectic composition between Fe_3C and Fe_7C_3, in accordance with the topology of Shterenberg et al. (1975). We preserve this general topology for Fe_7C_3 melting at higher pressures in the absence of further constraints. Overall, the topologies of phase relations in the pressure region of 5 to 10 GPa are drawn to be consistent in form with previous results (Nakajima et al., in press; Shterenberg et al., 1975; Strong and Chrenko, 1971; Tsuzuki et al., 1984).

We note that the position of invariant point I2 in Fig. 10 (~8 GPa) corresponds well with the inflection in the Fe_3C melting curve interpreted on the basis of the Kraut-Kennedy fits shown in

Fig. 4b. We speculate that this occurs because of the change in phase relations brought about by the emergence of Fe_7C_3 at the solidus, and a subsequent expansion of the Fe_7C_3 + liquid field with pressure as shown at 50 GPa in Fig. 9c. At 50 GPa the Fe_7C_3 melting point is about 500 K above that of Fe_3C, and we show an expansion of the Fe_7C_3 + liquid field and also infer a shift in Fe_3C peritectic melt composition to lower carbon contents. If true, this expansion of the Fe_7C_3 + liquid field necessitates that the change in partial molar volume of carbon in going from Fe_7C_3 to melt is positive. We also show that by 50 GPa the composition of the eutectic between Fe and Fe_3C is at less than 1 wt% carbon, as constrained by in situ measurements.

The Fe_3C and Fe–Fe_3C eutectic melting curves apparently converge at about 1.2 Mbar based on extrapolation of the Simon curves. The convergence of the Fe–Fe_3C eutectic with the $Fe_3C \rightarrow Fe_7C_3$ + liquid peritectic may occur because the melting point of pure Fe increases at a faster rate than does Fe_3C, eventually resulting in the breakdown of Fe_3C to Fe + Fe_7C_3 in the subsolidus. In *P-T* space this reflects another invariant point where the subsolidus reaction intersects the Fe_3C melting curve at which four phases coexist (Fe, Fe_3C, Fe_7C_3 and liquid), shown as I3 in Fig. 10 (See supplemental Fig. 3b). At pressures above the invariant point a new eutectic would form between Fe and Fe_7C_3, as shown in Fig. 9d. The composition of the eutectic is impossible to predict reliably but could be richer in carbon than the carbon-poor Fe–Fe_3C eutectic it replaces, with important implications for crystallization of Earth's inner core.

4.2 Constraints on Earth's Core

Although the Earth's metallic core is unlikely to be a binary Fe-C alloy, binary phase relations can be instructive as to the nature of phases that might have crystallized in the solid inner core, as well as to the relative concentration of carbon in the liquid outer core. For example, Wood (1993) predicted that Fe_3C would melt congruently at 136 GPa, and that the Fe–Fe_3C eutectic composition would be nearly pure Fe. On this basis Wood suggested that the inner core might have crystallized an Fe_3C phase, resulting in an outer core that would become carbon depleted as the

493 inner core crystallized, and predicted an inner core density that matches closely constraints from
494 seismology. Vocadlo et al. (2002), however, have convincingly showed on the basis of new elastic
495 parameters that nonmagnetic Fe_3C would have too low a density to match the inner core. Further,
496 Fiquet et al. (2009) have measured V_p in Fe_3C to 83 GPa and found it to be too high to match the
497 inner core. Indeed the authors estimate that the inner core can contain only ~1wt % carbon to satisfy
498 both the density and compressional wave velocity predicted by PREM. Using a similar technique,
499 Gao et al. (2008) determined both V_s and V_p up to 50 GPa, and found both to be larger than PREM
500 after extrapolation to core conditions, ruling out Fe_3C as a sole inner core phase, though the authors
501 suggest some lesser amount of carbon as an excellent candidate for reconciling the sound velocity
502 and density of Fe-Ni alloys with the measured values in the inner core.

503 Similar to the model of Wood (1993), we also find that the Fe-Fe_3C eutectic moves to nearly
504 pure Fe at high pressures. However, Wood has a steep *P-T* slope for the Fe_3C melting curve, which
505 results in congruent melting of Fe_3C at core pressures, effectively eliminating a role for Fe_7C_3. In
506 contrast, our phase relations, as well as those of Shterenberg et al. (1975) and Nakajima et al. (in
507 press), suggest an important role for Fe_7C_3 in the Fe-rich region of the phase diagram at high
508 pressures. Our results indicate that the melting point of Fe_7C_3 rapidly diverges from Fe_3C at high
509 pressure, and that the Fe_3C and eutectic melting curves converge (Fig. 10). These features conspire
510 to eliminate Fe_3C at the solidus, with replacement by Fe_7C_3 (Fig. 9d). Thus, the important point for
511 understanding the carbon partitioning between Earth's inner and outer core is the carbon content of
512 the eutectic formed between Fe and Fe_7C_3, as this together with the bulk core carbon content will
513 control the nature of the crystallizing phase in Earth's core.

514 The carbon content of Earth during core formation is poorly constrained, but likely is in the
515 range of 0.2 to 4 wt.%. If the predicted eutectic between Fe and Fe_7C_3 were close to pure iron, then
516 we would expect that for much of the predicted range of core carbon contents the inner core would
517 crystallize an Fe_7C_3 phase (Nakajima et al., in press). Little is known about the thermoelasticity of
518 this phase at core conditions, but we can predict that given its higher carbon content Fe_7C_3 might

519 provide a poor match for Earth's inner core, at least as a sole crystallizing phase. Conversely, if the
520 Fe–Fe_7C_3 eutectic is at moderate carbon contents as drawn in Fig. 9d, then the core could crystallize
521 a carbon-poor Fe phase, with the carbon content in the outer core increasing as crystallization
522 proceeds. In this case effectively all the core's carbon budget would reside in the liquid outer core.
523
524 **5. Conclusions**
525 We have measured the melting curves of Fe_3C, Fe_7C_3, and the Fe-Fe_3C eutectic up to ~70
526 GPa. We find a change in slope of the Fe_3C melting curve at ~8 GPa that corresponds with the
527 emergence of Fe_7C_3 at the solidus and the creation of a *P-T* invariant point. At pressures below the
528 invariant point our Fe_3C melting curve is consistent with that predicted from thermodynamic
529 calculations (Wood, 1993), but at pressures higher than the invariant point our melting curve
530 flattens and by 70 GPa is ~1000 K below that of Wood (1993). In contrast to Fe_3C, we find a steep
531 *P-T* slope for the Fe_7C_3 melting curve, and on this basis predict an expanding field of Fe_7C_3 + liquid
532 with pressure. Our measurements of the Fe-Fe_3C eutectic temperature are in close agreement with
533 the multi-anvil data of Fei et al. (2007) and to the thermodynamic calculations of Wood (1993). The
534 eutectic composition, measured in situ using a novel X-radiographic imaging technique, drops
535 rapidly with pressure, generally consistent with the prediction of Wood (1993), and has a
536 composition with less than 1% carbon by ~50 GPa. The resulting phase relations, though requiring
537 significant extrapolation to core pressures, suggest that Fe_3C will be replaced at the solidus by
538 Fe_7C_3 at ~120 GPa, thereby forming a new eutectic between Fe and Fe_7C_3. Until phase relations are
539 determined at megabar pressures and beyond we can only speculate regarding the nature of a
540 carbon-bearing phase that might be crystallizing in the inner core. For Fe_7C_3 to crystallize in the
541 inner core the proposed eutectic between Fe and Fe_7C_3 would have to be at a composition poorer in
542 carbon than the bulk core carbon content. We speculate that the opposite case is also possible, and
543 that the core carbon content is on the carbon-poor side of the eutectic such that carbon is expelled
544 nearly wholesale to the liquid outer core.

Acknowledgements

We thank J. Knight at ALS for technical support during the imaging experiments. RD acknowledges support of LDEO post-doctoral fellowship. OTL acknowledges support of a NERC PhD studentship. This work supported by NERC grant NE/C511548/1 to MJW and by NSF grants to DW. The Advanced Light Source is supported by the Director, Office of Science, Office of Basic Energy Sciences, of the U.S. Department of Energy under Contract No. DE-AC02-05CH11231. This research was partially supported by COMPRES, the Consortium for Materials Properties Research in Earth Sciences under NSF Cooperative Agreement EAR 06-49658.

555 **References**

556 Alfè, D., Price, G.D., Gillan, M.J., 2004. The melting curve of iron from quantum mechanics
557 calculations. J. Phys. Chem. 65, 1573-1580.

558 Alfè, D., Gillan, M.J., Price, G.D., 2002. Composition and temperature of the Earth's core by
559 combining ab initio calculations and seismic data. Earth Planet. Sci. Lett. 195, 91-98.

560 Anderson, O.L., Isaak, D.G., 2002. Another look at the core density deficit of Earth's outer core.
561 Phys. Earth Planet. Inter. 131, 19-27.

562 Badro, J., Fiquet, G., Guyot, F., Gregoryanz, E., Occelli, F., Antonangeli, D., d'Astuto, M., 2007.
563 Effect of light elements on the sound velocities in solid iron: Implications for the composition
564 of Earth's core. Earth Planet. Sci. Lett. 254, 233-238.

565 Benedetti, L.R., Guignot, L., Farber, D.L., 2007. Achieving accuracy in spectroradiometric
566 measurements of temperature in the laser-heated diamond anvil cell: Diamond as an optical
567 component. J. App. Phys. 101, 013109.

568 Birch, F., 1952. Elasticity and Constitution of Earth's Interior. J. Geophys. Res. 57, 227-286.

569 Birch, F., 1964. Density and composition of mantle and core. J. Geophys. Res. 69, 4377-4388.

570 Boehler, R., 2000. High pressure experiments and the phase diagram of lower mantle and core
571 materials. Rev. Geophys. 38, 221-245.

572 Boehler, R., Ross, M., Boercker, D.B., 1997. Melting of LiF and NaCl to 1 Mbar: Systematics of
573 Ionic Solids at Extreme Conditions. Phys. Rev. Lett. 78, 4589 – 4592.

574 Boehler, R., 1993. Temperatures in the Earth's core from melting point measurements of iron at
575 high static pressures. Nature. 363, 534-536.

576 Boehler, R., 1992. Melting of the Fe-FeO and Fe-FeS systems at high pressure – constraints on core
577 temperatures. Earth Planet. Sci. Lett. 111, 217-227.

578 Buffett, B.A., Garnero, E.J., Jeanloz, R., 2000. Sediments at the Top of Earth's Core. Science 290,
579 1338-1342.

580 Bundy, F.P., Bassett, W.A., Weathers, M.S., Hemley, R.J., Mao, H.K., Goncharov, A.F., 1994. The
581 pressure-temperature phase and transformation diagram for carbon; updated through 1994.
582 Carbon 34, 141-153.
583 Caldwell, W.A., Kunz, M., Celestre, R.S., Domning, E.E., Walter, M.J., Walker, D., Glossinger, J.,
584 MacDowell, A.A., Padmore, H.A., Jeanloz, R., Clark, S.M., 2007. Laser-heated diamond anvil
585 cell at the advanced light source beamline 12.2.2. Nuclear Instru. Meth. Phys. Res. A 582, 221-
586 225.
587 Campbell, A.J., Seagle, C.T., Heinz, D.L., Shen, G., Prakapenka, V.B. 2007. Partial melting in the
588 iron-sulfur system at high pressure: A synchrotron X-ray diffraction study. Phys. Earth Planet.
589 Int. 162, 119-128.
590 Chabot, N.L., Campbell, A.J., McDonough, W.F., Draper, D.S., Agee, C.B., Humayan, M., Watson,
591 H.C., Cottrell, E., Saslow, S.A., 2008. The Fe-C system at 5 GPa and Implications for Earth's
592 Core. Geochim. Cosmochim. Acta. 72, 4146-4148.
593 Chabot, N.L., Campbell, A.J., Jones, J.H., Humayan, M., Lauer Jr., V.L., 2006. The influence of
594 carbon on trace element partitioning behavior. Geochim. Cosmochim. Acta. 70, 1322-1335.
595 Chipman, J., 1972. Thermodynamics and Phase Diagram of the Fe-C System. Metal. Trans. 3,
596 1972-55.
597 Dasgupta, R., Walker, D., 2008. Carbon Solubility in Core Melts in a Shallow Magma Ocean
598 Environment and Distribution of Carbon between the Earth's Core and the Mantle. Geochim.
599 Cosmochim. Acta. 72, 4627-4641.
600 Dewaele, A., Mezouar, M., Guignot, N., Loubeyre, P., 2007. Melting of lead under high pressure
601 studied using second-scale time-resolved x-ray diffraction. Phys. Rev. B. 76, 144106.
602 Dewaele, A., Loubeyre, P., Occelli, F., Mezouar, M., Dorogokupets, P. I., Torrent, M., 2006.
603 Quasihydrostatic Equation of State of Iron above 2 Mbar. Phys. Rev. Lett. 97, 215504.

604 Dubrovinsky, L.S., Saxena, S.K., Tutti, F., Rekhi, S., LeBehan, T., 2000. In situ X-ray Study of
605 Thermal Expansion and Phase Transition of Iron at Multimegabar Pressure. Phys. Rev. Lett.
606 84, 1720-1723.
607 Dubrovinsky, L.S., Annersten, H., Dubrovinskaia, N., Westman, F., Harryson, H., Fabrichnaya, O.,
608 Carlson, S., 2001. Chemical interaction of Fe and Al_2O_3 as a source of heterogeneity at the
609 Earth's core-mantle boundary. Nature 412, 527-529.
610 Duman, E., Acet, M., Wassermann, E. F., Itié, J. P., Baudelet, F., Mathon, O., Pascarelli, S., 2005.
611 Magnetic Instabilities in Fe_3C Cementite Particles Observed with Fe K-Edge X-Ray Circular
612 Dichroism under pressure. Phys. Rev. Lett. 94, 075502.
613 Fei, Y., Wang, Y., Deng, L., 2007. Melting relations in the Fe-C-S system at high pressures:
614 Implications for the chemistry of the cores of the terrestrial planets. Lunar and Planetary
615 Science Conference XXXVIII abstract 1231.
616 Gao, L., Chen, B., Wang, J., Alp, E. E., Zhao, J., Lerche, M., Sturhahn, W., Scott, H. P., Huang, F.,
617 Ding, Y., Sinogeikin, V., Lundstrom, C. C., Bass, J. D., Li, J., 2008. Pressure-induced magnetic
618 transition and sound velocities of Fe_3C: Implications for carbon in the Earth's inner core. Geo.
619 Res. Lett. 35, L17306.
620 Goodrich, C.A., 1992. Ureilites – A Critical Review. Meteoritics. 27, 327-352.
621 Häglund, J., Grimvall, G., Jarlborg, T., 1991. Electronic structure, x-ray photoemission spectra, and
622 transport properties of Fe_3C (cementite). Phys. Rev. B. 44, 2914-2919.
623 Heinz, D.L., Jeanloz, R., 1987. Temperature measurement in the laser heated diamond cell. In:
624 Manghnani, M.H., Syono, Y. (Eds). High-Pressure Research in Mineral Physics, Vol. 39,
625 Geophysical Monograph ser. 39. American Geophysical Union, Washington, DC, pp. 393-492.
626 Hillgren, V.J., Gessmann, C.K., Li, J., 2000. An experimental perspective on the light element in
627 the Earth's core, in: Canup, R.M., Righter, K. (Eds). Origin of the Earth and Moon. The
628 University of Arizona Press, Tucson.

629 Hirayama, Y., Fujii, T., Kurita, K., 1993. The melting relation of the system, iron and carbon at
630 high-pressure and its bearing on the early-stage of the Earth. Geophys. Res. Lett. 20, 2095-
631 2098.
632 Hofmeister, A.M., Mao, H.K., 2003. Pressure derivatives of shear and bulk moduli from the thermal
633 Grüneisen parameter and volume-pressure data. Geochim. Cosmochim. Acta 67, 1215-1235.
634 Jana, D., Walker, D., 1997. The impact of carbon on element distribution during core formation.
635 Geochim. Cosmochim. Acta 61, 2759-2763.
636 Javoy, M., 1997. The major volatile elements of the Earth: Their origin, behavior and fate.
637 Geophys. Res. Lett. 24, 177-180.
638 Kavner, A., Jeanloz, R., 1998. High pressure melting curve of platinum. J. App. Phys. 83, 7553-
639 7559.
640 Kavner, A., Panero, W. R., 2004. Temperature gradients and evaluation of thermoelastic properties
641 in the synchrotron-based laser-heated diamond cell. Phys. Earth. Planet. Inter. 143-144, 527-
642 539.
643 Kraut, E.A., Kennedy, G.C., 1966. New melting law at high pressures. Phys. Rev. Lett. 16, 608-
644 609.
645 Li, J., Fei, Y., 2003. Experimental constraints on core composition. In: Carlson, R.W. (Ed.), The
646 Mantle and Core. Elsevier-Pergammon, Oxford. 2, 521-546.
647 Lin, J.-F., Struzhkin, V. V., Mao, H.-K., Hemley, R. J., Chow, P., Hu, M. Y., Li, J., 2004. Magnetic
648 transition in compressed Fe_3C from x-ray emission spectroscopy. Phys. Rev. B 70, 212405.
649 Lister, J.R., Buffett, B.A., 1998. Stratification of the outer core at the core-mantle boundary. Phys.
650 Earth Planet. Inter. 105, 5-19.
651 Lodders, K., 2003. Solar system abundances and condensation temperatures of the elements.
652 Astrohphys. J. 591, 1220-1247.
653 Luo, S.N., Ahrens, T.J., 2004. Shock-induced superheating and melting curves of geophysically
654 important minerals. Phys. Earth Planet. Inter. 143-144, 369-386.

655 Ma, Y., Somayazulu, M., Shen, G., Mao, H.K., Shu, J., Hemley, R. J., 2004. In Situ X-ray
656 Diffraction studies of iron to Earth-core conditions. Phys. Earth Planet. Inter. 143-144, 455-
657 467.
658 Mao, H.K., Wu, Y., Chen, L.C., Shu, J.F., 1990. Static Compression of Iron to 300 GPa and
659 $Fe_{0.8}Ni_{0.2}$ Alloy to 260 GPa: Implications for Composition of the Core. J. Geophys. Res. 95,
660 21737-21742.
661 Mao, H.K., Xu, J., Bell, P.M., 1986. Calibration of the ruby pressure gauge to 800 kbar under quasi-
662 hydrostatic conditions. J. Geophys. Res. 91, 4673-4676.
663 McDonough, W.F., 2003. Compositional Model for the Earth's Core, in: Carlson, R.W. (Ed.), The
664 Mantle and Core. Elsevier-Pergammon, Oxford.
665 McDonough, W.F., Sun, S.S., 1995. The composition of the Earth. Chem. Geol. 120, 223-253.
666 Nakajima, T., Takahashi, E., Suzuki, T., Funakoshi, K.I., Accepted Manuscript. "Carbon in the
667 core" revisited. Phys. Earth Planet. Inter.
668 O'Neill, H.St.C., Canil, D., Rubie, D.C., 1998. Oxide-metal equilibria to 2500°C and 25 GPa:
669 Implications for core formation and the light component in the Earth's core. J. Geophys. Res.
670 103, 12239-12260.
671 Poirier, J.P., 1994. Light elements in the Earth's outer core – A critical review. Phys. Earth Planet.
672 Inter. 85, 319-337.
673 Ringwood, A.E., Hibberson, W., 1990. The System Fe – FeO Revisited. Phys. Chem. Min. 17, 313-
674 319.
675 Rouquette, J., Dolejs, D., Kantor, I.Y., McCammon, C.A., Frost, D.J., Prakapenka, V.B.,
676 Dubrovinsky, L.S. 2008. Iron-carbon interactions at high temperatures and pressures. App.
677 Phys. Lett. 92, 121912.
678 Seagle C.T., Heinz D.L., Campbell A.J., Prakapenka V.B., Wanless S.T., 2008. Melting and
679 thermal expansion in the Fe-FeO system at high pressure. Earth Planet. Sci. Lett. 265, 655-665.

680 Shanker, J., Singh, B.P., Srivastava, S.K., 2004. Volume-temperature relationship for iron at 330
681 GPa and Earth's core density deficit. Phys. Earth. Planet. Inter. 147, 333-341.
682 Shen, G., Prakapenka, V. B., Rivers, M. L., Sutton, S. R., 2004. Structure of Liquid Iron at
683 Pressures up to 58 GPa. Phys. Rev. Lett. 92, 185701.
684 Shen, G., Mao, H.K., Hemley, R.J., Duffy, T.S., Rivers, M.L., 1998. Melting and crystal structure
685 of iron at high pressures and temperatures. Geophys. Res. Lett. 25, 373-376.
686 Simon, F., Glatzel, G., 1929. Remarks on fusion pressure curve. Z. Anorganische Allgemeine
687 Chem. 178, 309-316.
688 Shterenberg, L.E., Slesarev, V.N., Korsunskaya, I.A., Kamenetskaya, D.S., 1975. The experimental
689 study of the interaction between melt, carbides and diamond in the iron – carbon system at high
690 pressures. High Temperatures – High Pressures 7, 517-522.
691 Strong, H.M., Chrenko, R.M., 1971. Further Studies on Diamond Growth Rates and Physical
692 Properties of Laboratory-Made Diamonds. J. Phys. Chem. 75, 1838-1843.
693 Tsuzuki, A., Sago, S., Hirano, S.I., Naka, S., 1984. High temperature and pressure preparation and
694 properties of iron carbides Fe_7C_3 and Fe_3C. J. Mat. Sci. 19, 2513-2518.
695 Walker, D., Lord, O.T., Walter, M.J., Clark, S.M., 2009. X-ray absorption contrast images of binary
696 chemical reactions. Chem. Geol. 260, 211-220, doi:10.1016/j.chemgeo.2008.12.025.
697 Walker, D., 2005. Core-mantle chemical issues. Canad. Min. 43, 1553-1564.
698 Walter, M.J., Koga, K.T., 2004. The effects of chromatic dispersion on temperature measurement in
699 the laser-heated diamond anvil cell. Phys. Earth Planet. Inter. 143-144, 541-558.
700 Weast, R.C., Astle, M.J., Beyer, W.H. (Eds), 1985. Handbook of Chemistry and Physics. CRC
701 Press Inc., Boca Raton, Florida.
702 Wood, B.J., 1993. Carbon in the core? Earth Planet. Sci. Lett. 117: 593-607.
703 Wood, I.G., Vocadlo, L., Knight, K.S., Dobson, D.P., Marshall, W.G., Price, G.D., Brodholt, J.,
704 2004. Thermal expansion and crystal structure of cementite, Fe_3C, between 4 and 600 K
705 determined by time-of-flight neutron powder diffraction. J. App. Crystal. 37, 82-90.

706 Vocadlo, L., Brodholt, J., Dobson, D.P., Knight, K.S., Marshall, W.G., Price, G.D., Wood, I.G.,
707 2002. The effect of ferromagnetism on the equation of state of Fe_3C studied by first-principles
708 calculations. Earth Planet. Sci. Lett. 203, 567-575.
709

710 **Figure Captions**

711 Fig. 1. The iron rich portion of the Fe-C phase diagram at 1 atmosphere after Chipman (1972) and
712 at 5.7 GPa after Strong and Chrenko (1971). The dashed line in the 1 atmosphere diagram indicates
713 that the liquid + Fe_3C field is metastable. The arrow at 8.41 wt% C indicates the location of Fe_7C_3,
714 which does not become stable until higher pressure. L = liquid; Gr = graphite; Di = diamond.

715

716 Fig. 2. Typical power vs. temperature functions from Fe_3C melting experiments. (a-b) In these two
717 cases the temperature plateaus with increasing power, and the melting point is taken as the average
718 of the points within the plateau, while the error bars represent their standard deviation. (c) In this
719 less common example, the temperature drops suddenly on melting. Here, a linear fit to the power
720 vs. temperature function is extrapolated to the next acquisition. The melting temperature is taken as
721 the center point between this and the previous measured temperature, with the uncertainty
722 encompassing the two points. Within each experiment, care was taken to ensure the time between
723 acquisitions remained constant, and is on the order 5-20 seconds in most experiments. Uncertainty
724 due to the precision of temperature measurement is smaller than the symbol size in all cases. Each
725 acquisition number (x-axis) represents an increase in laser current; the increments are equal, and so
726 the axis is simply a proxy for power, which was not directly measured.

727

728 Fig. 3. Melting data for FeS (open diamonds), Fe (open squares), Pt (open circles) and Pb (open
729 triangles) using our laser DAC, temperature measurement techniques and melting criteria. Our data
730 is compared to literature melting data as a test of consistency. Solid line, DAC melting data for FeS
731 from Boehler (1992); filled squares, multi anvil melting point of iron from Ringwood and
732 Hibberson (1990); short dashed line, DAC melting data for Fe from Boehler (1993); dotted line,
733 DAC melting data for Pt from Kavner and Jeanloz, (1998) and long dashed line, DAC melting data
734 for Pb from Dewaele et al. (2007).

735

736 Fig. 4. The Fe_3C melting curve. (a) Melting temperatures from DAC laser heating experiments
737 (open circles, Bristol; closed circles, ALS) and melting brackets from piston cylinder and multi
738 anvil quench experiments (closed triangles) are shown. The solid line is a fit to the data, excluding
739 the anomalously low point at 60 GPa, using the empirically derived Simon equation, and the dotted
740 line indicates the Fe_3C melting curve from the thermodynamic calculations of Wood (1993). The
741 long dashed line represents the multi-anvil melting data of Nakajima et al. (in press). The inset (b)
742 shows the low-pressure region of the melting curve from (a) expanded for clarity, illustrating the
743 close agreement between DAC and large volume press melting data. The 2 GPa piston cylinder data
744 were previously reported in Dasgupta and Walker (2008), and along with the multi-anvil data at 5
745 and 6 GPa have uncertainties in temperature and pressure much smaller than the symbol size. (c)
746 Melting data plotted against isothermal compression of the paramagnetic phase of Fe_3C. The
747 compression has been calculated using a 3rd order Birch-Murnaghan Equation of State and the
748 calculated parameters $V_{0,483}$, $K_{0,483}$ and $K'_{0,483}$ taken from Vocadlo et al. (2002). The solid lines are
749 fits to the data using the Kraut-Kennedy equation (Kraut and Kennedy, 1966). The low pressure
750 curve was fitted to the black circles, the high pressure curve to the white ones, while the grey
751 symbols were included in both fits. Note the inflexion around a compression value of 0.03. We
752 interpret this as possibly representing a change in the peritectic melting reaction from $Fe_3C \rightarrow$
753 liquid + diamond to $Fe_3C \rightarrow$ liquid + Fe_7C_3, which also produces an invariant point in P-T space
754 (~8 GPa). The grey region represents an estimate of uncertainty on the position of this invariant
755 point.
756
757 Fig. 5. Melting curves of Fe_7C_3 and the Fe-Fe_3C eutectic. The eutectic melting curve is determined
758 from LH-DAC experiments using the 'donut' technique for melting at a boundary between spatially
759 resolved ingredients (open circles, Bristol; closed circles, ALS). The data are fitted to a Simon
760 equation (solid line). The dotted line is the calculated eutectic curve of Wood (1993), the dashed
761 line is a linear fit to the multi anvil quench data of Fei et al. (2007), and the dash-dot line a linear fit

762 to the data of Hirayama et al. (1993). The solid squares show melting determinations for Fe_7C_3,
763 which have been fitted with a Simon equation.
764
765 Fig. 6. Sequence of temperature profiles acquired during heating at the boundary between Fe and
766 Fe_3C, with an approximate boundary denoted by the dashed line. At first the temperature in the
767 Fe_3C is higher than the iron, as it more readily absorbs the laser radiation (lightest grey line). As
768 laser power is increased the temperature rises and then plateaus around 1900 K, indicating melting
769 has occurred. Simultaneously, the temperature of the Fe rises, until it equalizes with the Fe_3C
770 temperature, suggesting the formation of a homogenous melt pool at the boundary. These data were
771 acquired simultaneously with X-radiographic images of the boundary region, which show the
772 formation of the melt (see figure 7b).
773
774 Fig. 7. Examples of cross sections from X-radiographic images of Fe-Fe_3C 'donuts' used to
775 determine eutectic composition. The left hand panel in each case shows the initial boundary at 300
776 K before laser heating. The X-ray transmissivity is higher on the left (the Fe_3C) than the right (the
777 Fe) (a) 10 GPa: In the right hand panel, during in situ laser heating, a small but well-defined ledge
778 has formed, representing the presence of a eutectic melt. (b) 19 GPa: The ledge in the example
779 formed at 1875 K, simultaneously with a plateau in the measured temperature (see figure 6). The
780 contrast between the iron and Fe_3C is larger in this example than the others, because the exposure
781 time was longer. (c) 27 GPa: In this case, the ledge formed at 2160 K. For the sake of clarity, in
782 each panel the y-axis scaling has been altered so that the positions of the lines representing the
783 transmissivity of Fe and Fe_3C line up across the diagram.
784
785 Fig. 8. The pressure dependence of the Fe-Fe_3C eutectic as determined by in situ LH-DAC X-
786 radiographic imaging. Error bars represent the estimated uncertainty in finding the plateau position,
787 except where this is smaller than the uncertainty due to the detection limit. The filled diamond

represents an experiment at 44 GPa which yielded no ledge during heating, suggesting the solubility may have dropped to less than the detection limit; the error bar encompasses the noise within the Fe baseline where a plateau might be hidden. The open circles and open square represent the multi-anvil quench data of Hirayama et al. (1993) and Chabot et al. (2008), respectively. The filled square indicates the 1 atmosphere eutectic from Chipman (1972).

Fig. 9. The Fe-rich portion of the Fe-C phase diagram at 5, 10, 50 and 130 GPa, inferred from measurements of the melting curves of Fe_3C, Fe_7C_3 and the Fe-Fe_3C eutectic, as well as eutectic compositions determined from X-radiographic imaging experiments. The melting curve of iron is from Shen et al. (1998; 2004). L, liquid; Gr, graphite; Di, diamond; Values in italics represent melting temperatures and those in bold represent compositions. Dashed lines are used where the phase relations are inferred.

Fig. 10. Pressure-temperature phase diagram for Fe_3C (the Fe-Fe_3C melting curve is also shown as grey line). Construction and symbols as in Figure 9. Filled circles represent *P-T* invariant points. Point I1 represents the intersection of the graphite + liquid to diamond + liquid curve with the Fe_3C melting curve. Point I2 represents a change in the Fe_3C peritectic reaction products from diamond + liquid below ~8 GPa to Fe_7C_3 + liquid at higher pressures. Point I3 represents the predicted intersection between the Fe_3C and Fe-Fe_3C melting curves, at which point a new *P-T* invariant forms that also corresponds to the elimination of Fe_3C at the solidus (also shown as a dashed line is a subsolidus univariant reaction where Fe_3C breaks down to Fe + Fe_7C_3). At pressures higher than point I3, Fe_3C composition melts at a new eutectic between Fe and Fe_7C_3. The graphite to diamond transition is after Bundy et al. (1994).

Supplemental Fig. 1. A typical spectroradiometric temperature measurement for Fe_7C_3 at 52 GPa in the laser heated diamond cell. (a) Normalised intensity (J) vs. normalized wavelength (ω), where

814 $c_1 = 2\hbar c^2$ and $c_2 = \hbar c / k$ (c, speed of light; $\hbar$, Planck's constant; k, Boltzman's constant). Each curve
815 represents the system response to the incandescent light emitted from a region along a transect
816 across the laser heated spot, fitted using the Wien approximation. (b) A fit to each wavelength-
817 intensity spectrum yields a temperature, which is used to produce a cross-section. The fitting error
818 averaged over all points in the profile is 5.6 K. For a melting determination, the peak temperature is
819 used, which in this case is 3280 K. Fitting the data using the Wien approximation (solid line) and
820 Planck function (dashed line) yield temperatures which deviate by only ~20 K at ~3300 K.
821
822 Supplemental Fig. 2. Determination of metal melting points at 1 atm using resistance heating and
823 spectroradiometry. The filled circles represent replicate analyses except for Nb and Ta, which
824 represent a single analysis. The solid line indicates the expected 1:1 correspondence between
825 known and measured melting points. In all cases the symbol size is larger than the error bars. The
826 markers on the right hand y-axis indicate the melting points as derived from the literature (Weast et
827 al., 1985).
828
829 Supplemental Fig. 3. The phase reaction topology around invariant points I2 and I3 in Figure 10.
830 Di, diamond; L, liquid. Solid lines are univariant equilibria and dashed lines are their metastable
831 extensions. The phase in parentheses labeling each univariant curve is the 'phase out' in the given
832 reaction.
833

834 **Figure 1**

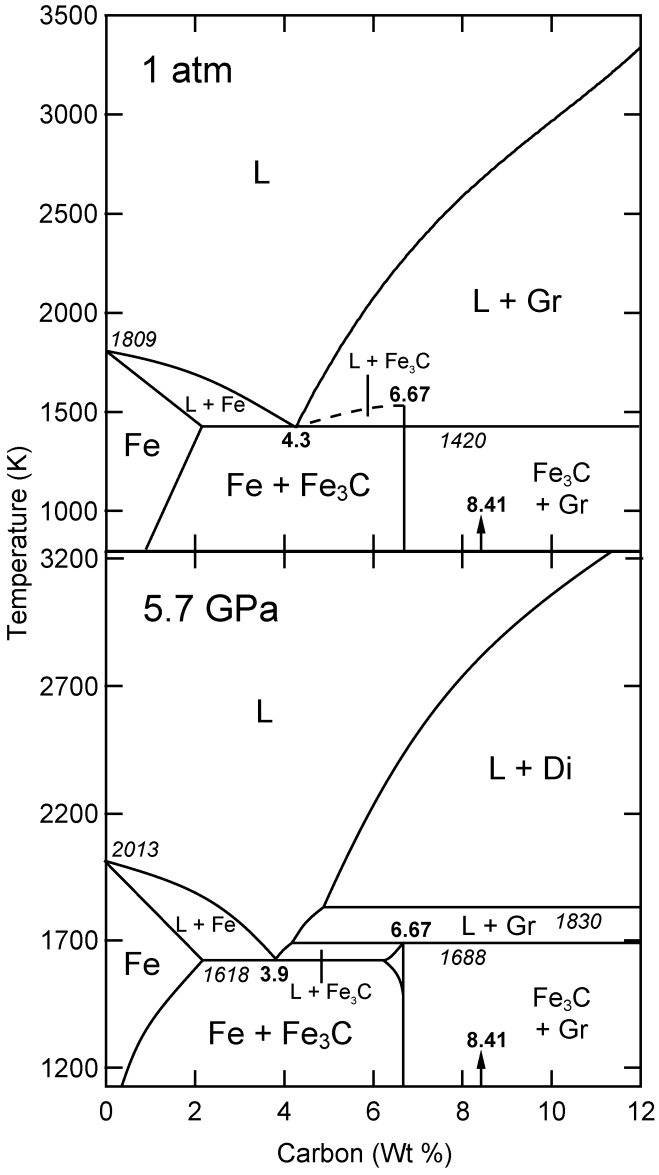

835

836

837 **Figure 2**

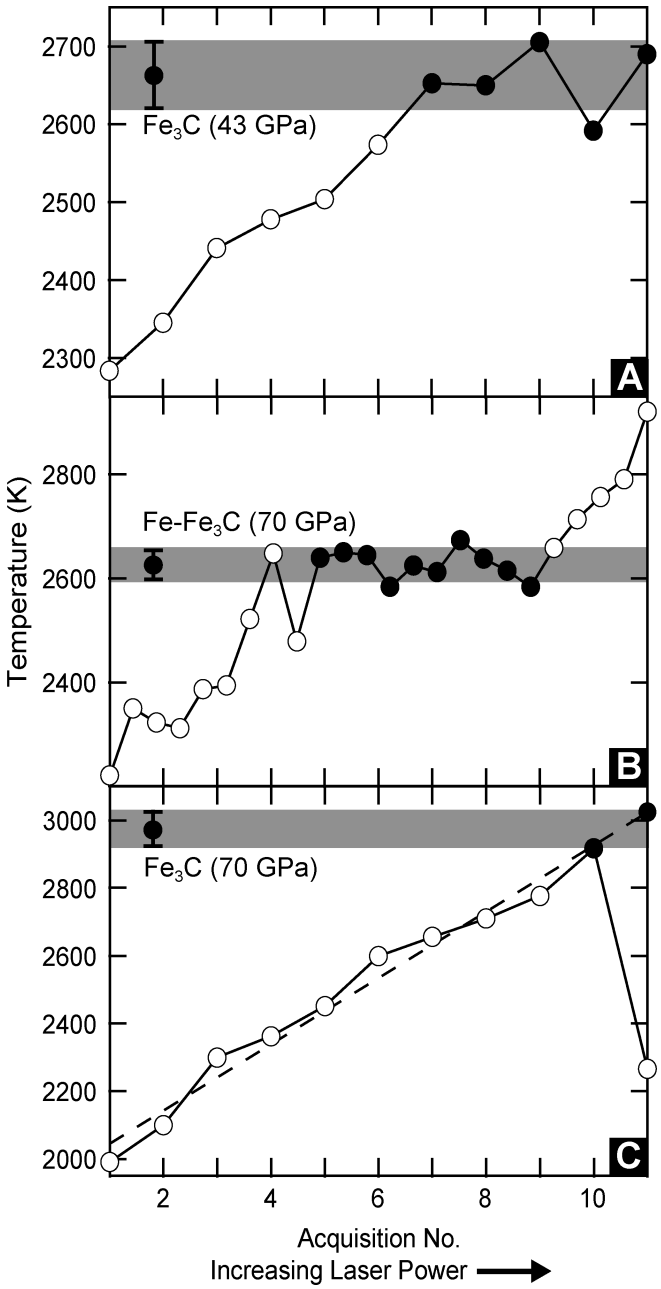

838

839

840 **Figure 3**

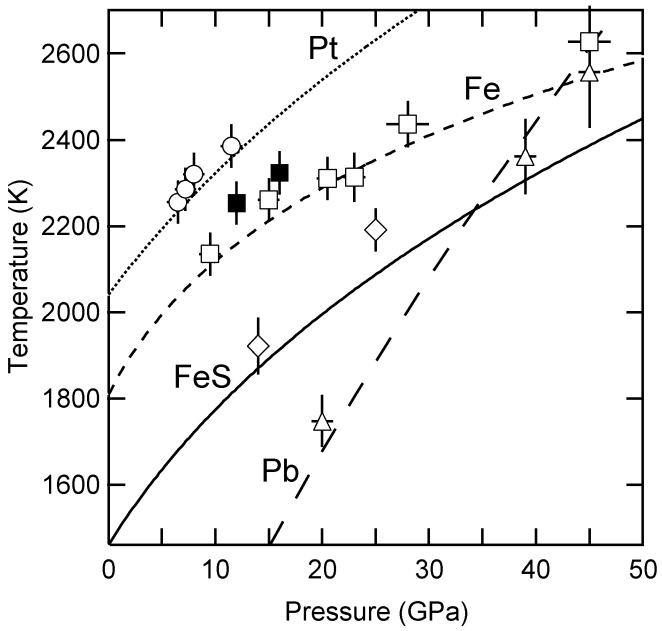

841

842

843 **Figure 4**

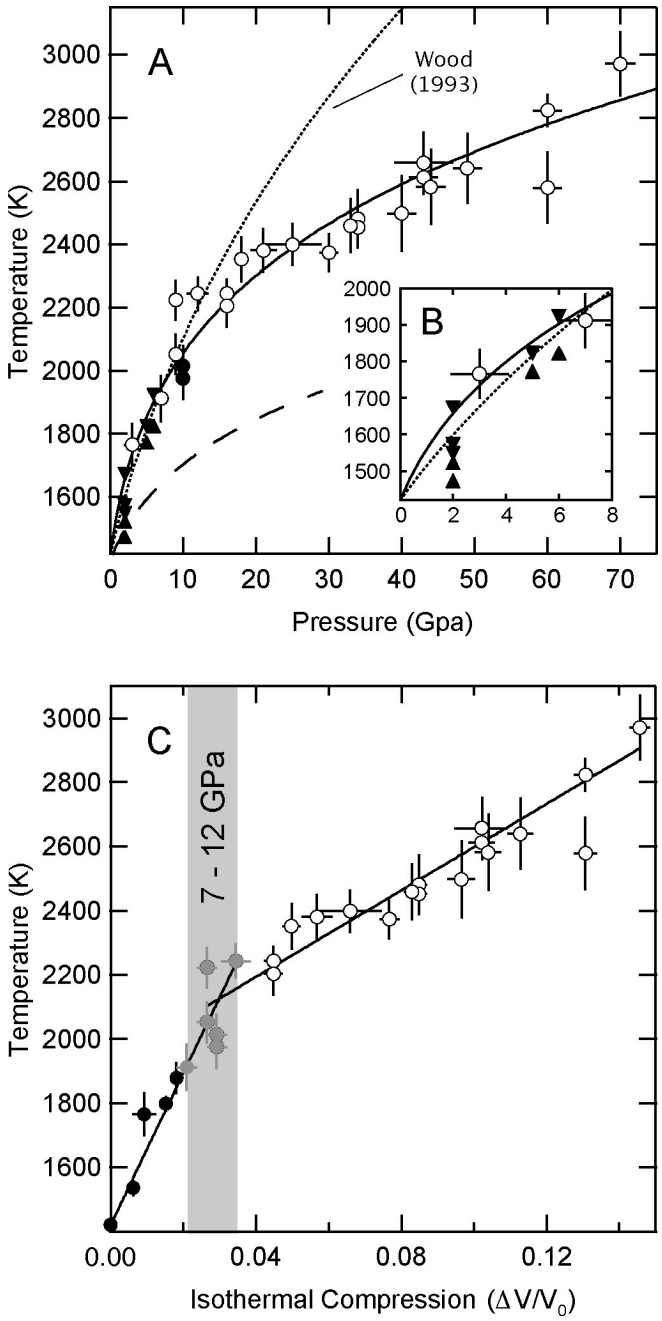

844

845

846 **Figure 5**

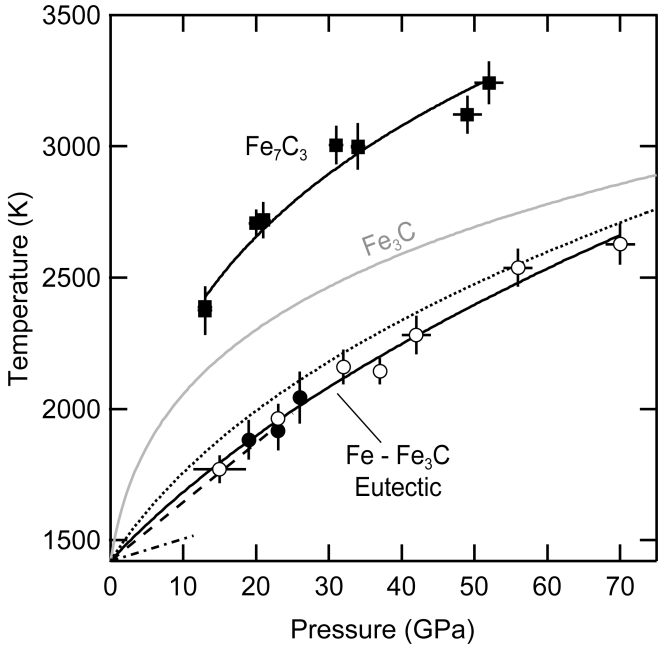

847

848

849 **Figure 6**

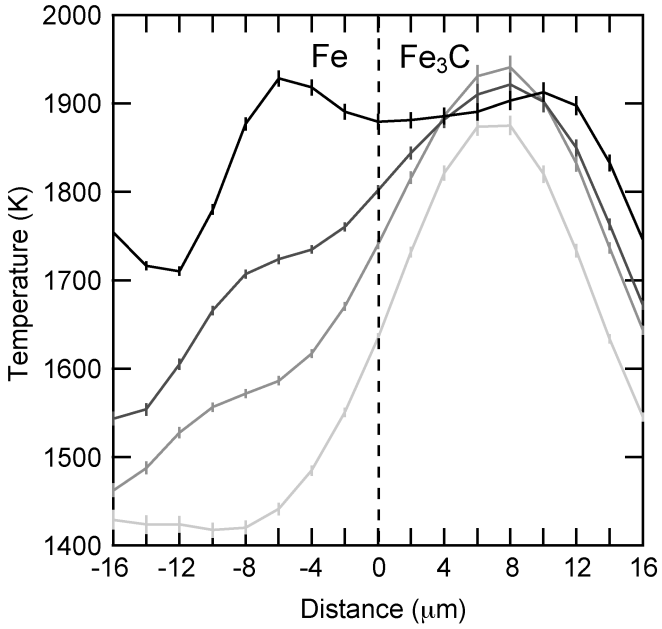

850

851

852 **Figure 7**

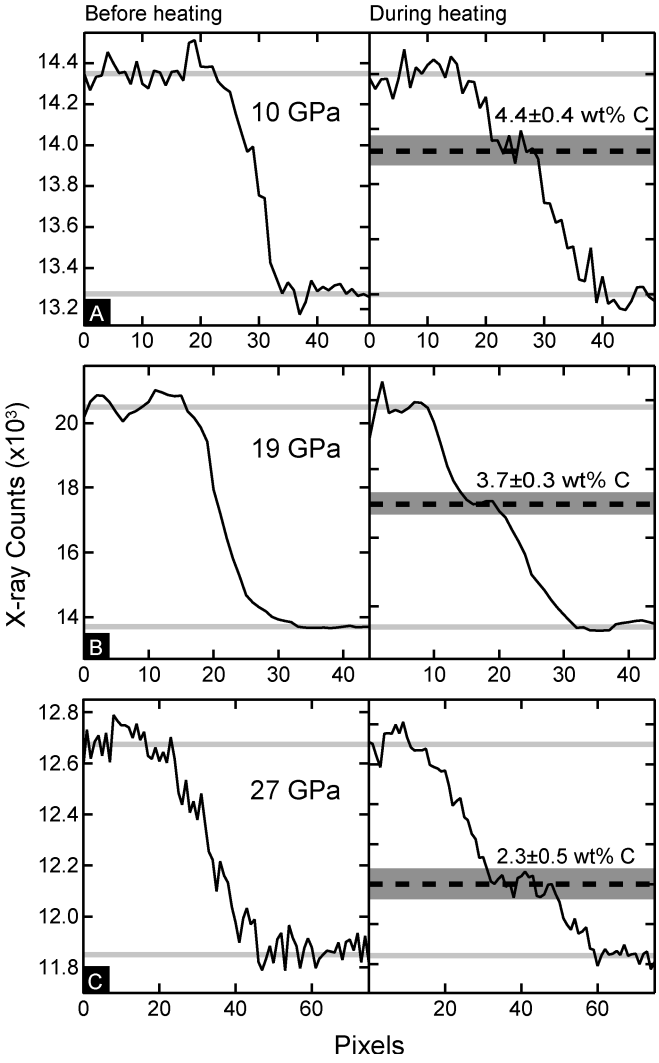

853

854

855 **Figure 8**

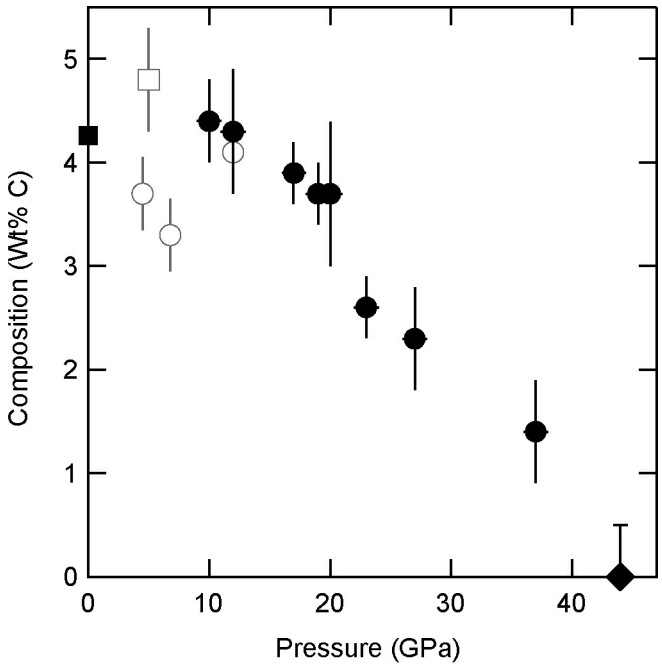

856

857

858 **Figure 9**

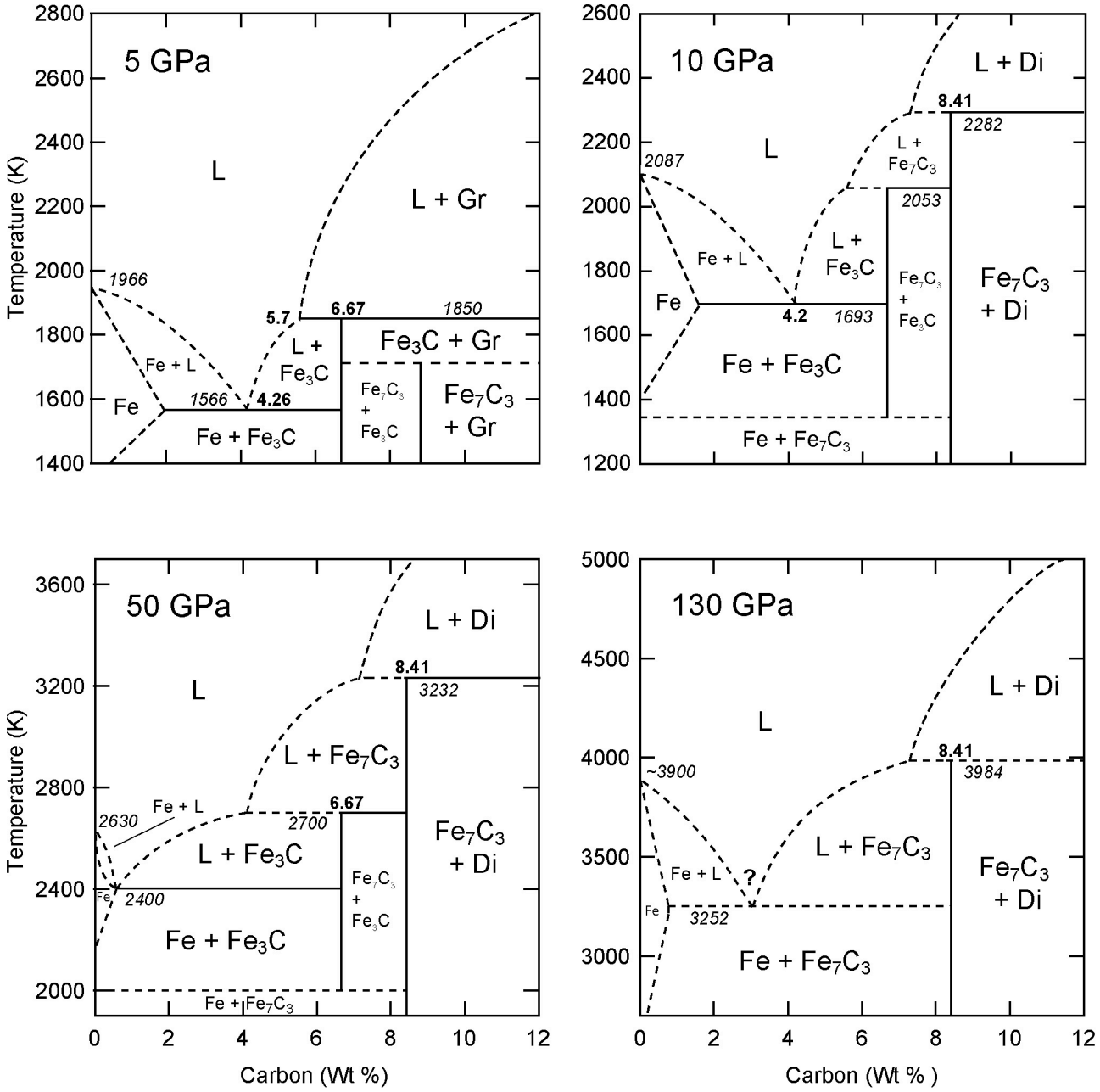

859

860

861 **Figure 10**

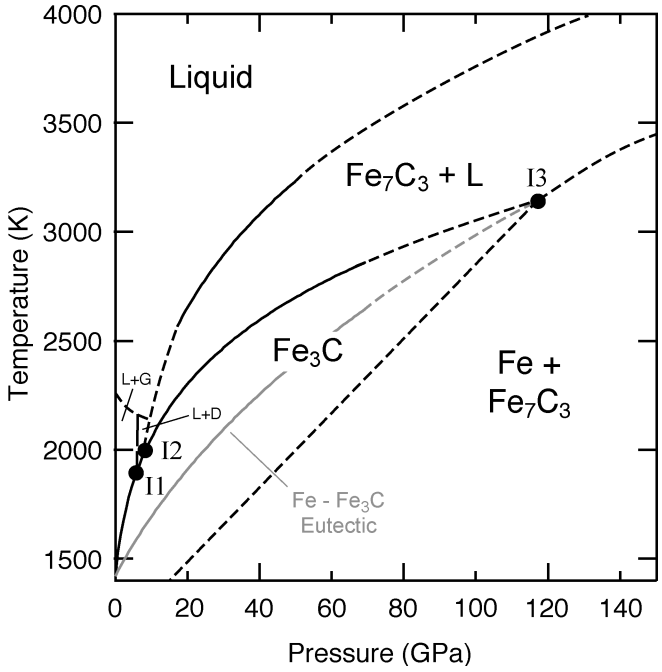

862

863

Supplemental Figure 1

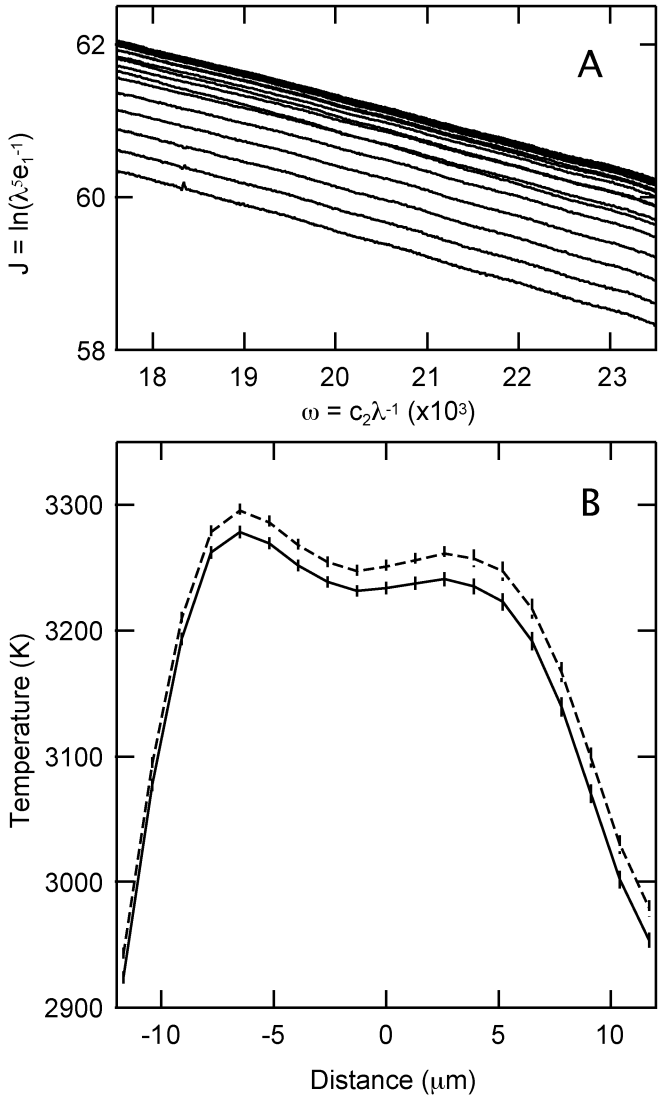

867 **Supplemental Figure 2**

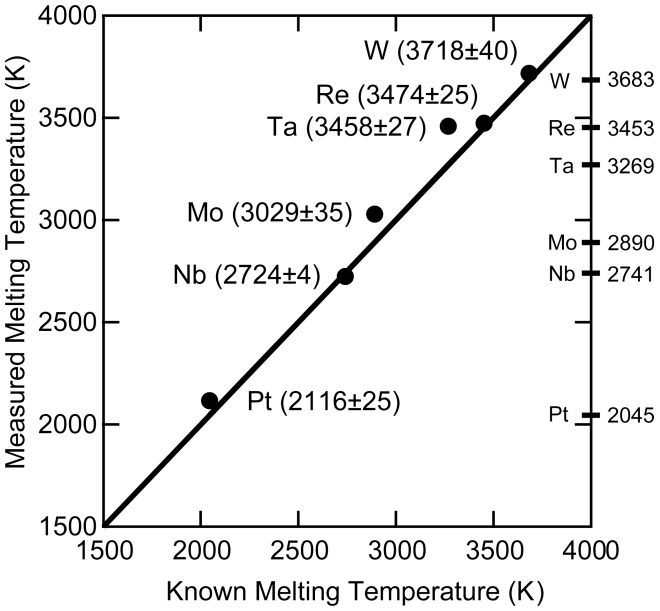

868

869

Supplemental Figure 3

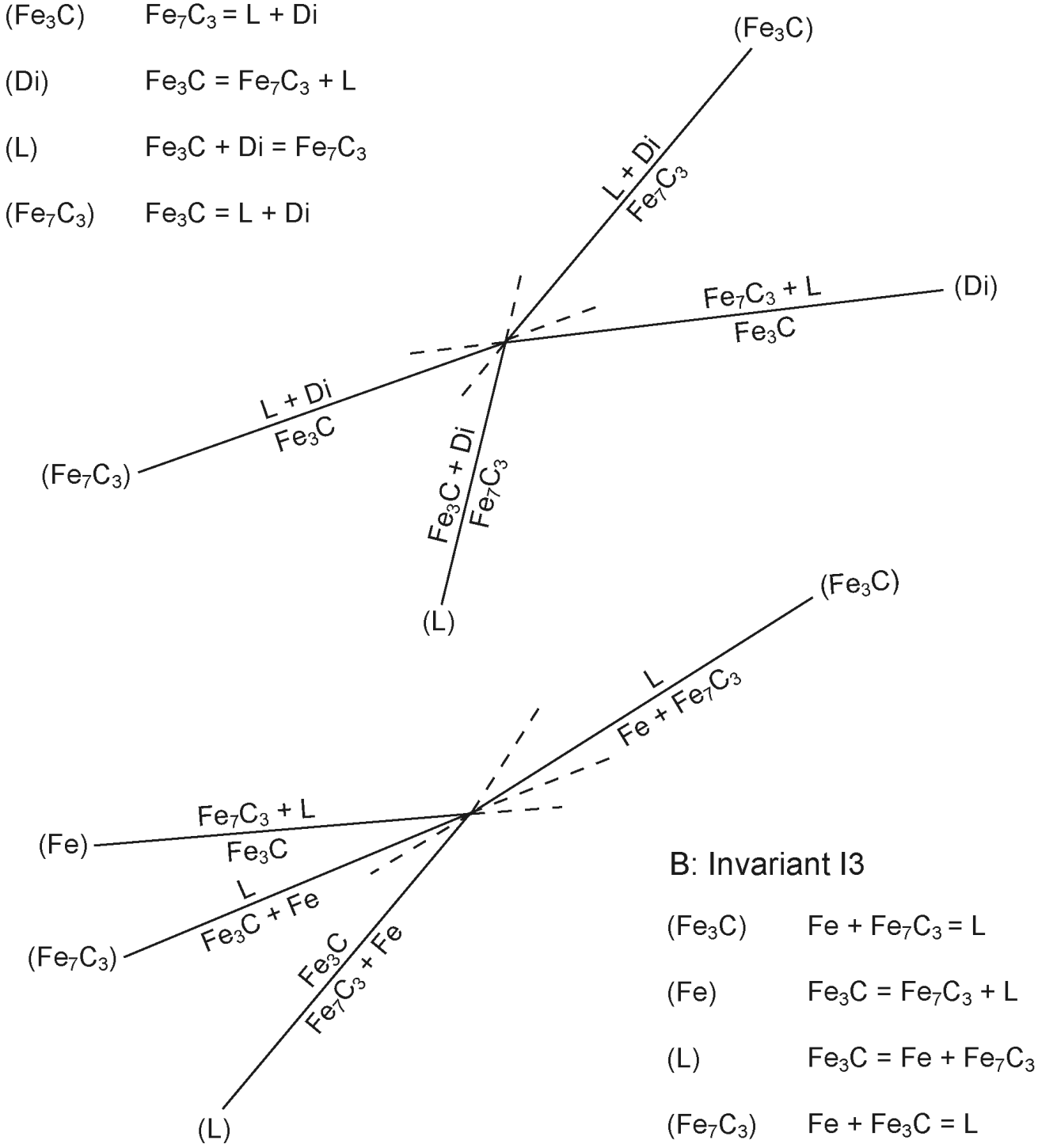

873 **Supplemental Table**

Table 1: Experimental run conditions

Run	Location	Pressure (GPa)	Temperature (K)
Fe_3C			
RD3[a]	LDEO	2 ± 0.1	1536 ± 15
07E	Bristol	3 ± 1.1	1766 ± 69
MA1[a]	LDEO	5 ± 0.5	1798 ± 25
MA2[a]	LDEO	6 ± 0.5	1878 ± 50
22A	Bristol	7 ± 1.0	1912 ± 75
14B	Bristol	9 ± 1.0	2052 ± 65
21E	Bristol	9 ± 1.0	2223 ± 65
XRD03	ALS	10 ± 1.0	2014 ± 67
XRD04	ALS	10 ± 1.0	1976 ± 69
07C	Bristol	12 ± 1.5	2243 ± 54
14D	Bristol	16 ± 1.0	2244 ± 47
14E	Bristol	16 ± 1.0	2204 ± 68
07G	Bristol	18 ± 1.0	2352 ± 73
07D	Bristol	21 ± 1.8	2381 ± 71
06A	Bristol	25 ± 4.0	2399 ± 68
23A	Bristol	30 ± 1.3	2374 ± 62
XRD06A	Bristol	33 ± 1.0	2459 ± 87
04B	Bristol	34 ± 1.0	2481 ± 94
04C	Bristol	34 ± 1.0	2453 ± 60
01	Bristol	40 ± 2.0	2498 ± 122
05	Bristol	43 ± 2.0	2612 ± 56
10A	Bristol	43 ± 4.0	2658 ± 98
06B	Bristol	44 ± 2.0	2582 ± 121
12C	Bristol	49 ± 2.0	2640 ± 112
12B	Bristol	60 ± 2.0	2824 ± 53
03	Bristol	70 ± 2.0	2971 ± 103
Fe_7C_3			
03B	Bristol	13 ± 1.0	2388 ± 75
03C	Bristol	13 ± 1.0	2375 ± 93
09D	Bristol	20 ± 1.0	2707 ± 53
09E	Bristol	21 ± 1.0	2719 ± 69
04C	Bristol	31 ± 1.0	3004 ± 73
08D	Bristol	34 ± 1.0	2997 ± 69
08E	Bristol	34 ± 1.0	3000 ± 88
12C	Bristol	49 ± 2.0	3122 ± 72
12D	Bristol	52 ± 2.0	3242 ± 82
Fe-Fe_3C			
05B	Bristol	15 ± 3.6	1770 ± 52
36B	ALS	23 ± 1.0	1916 ± 73
37A	ALS	19 ± 1.0	1881 ± 76
03A	Bristol	23 ± 1.0	1963 ± 56
39A	ALS	26 ± 1.0	2042 ± 99
03B	Bristol	32 ± 1.0	2159 ± 67
02	Bristol	37 ± 1.0	2143 ± 50
01	Bristol	42 ± 2.0	2281 ± 74
04A	Bristol	56 ± 2.0	2538 ± 74
04B	Bristol	70 ± 2.0	2627 ± 79

[a]Data points RD3 (piston cylinder), MA1 and MA2 (multi-anvil) each represent the center point of a bracket, and are not single experiments. See section 3.1 of the main text for details.

874